nature communications

Article

https://doi.org/10.1038/s41467-025-63923-z

Plasma-electrocatalytic synthesis of urea from air and CO2

Received: 12 April 2025

Accepted: 2 September 2025

Published online: 03 October 2025

Check for updates

Zeyi Sun[1], Rui Niu[1], Shiyao Shang[1], Yali Guo[1], Hu Zhang[2], Xijun Liu[3] ✉, Libang Feng[1] ✉ & Ke Chu[1] ✉

Electrochemical C-N coupling of CO_2 with nitrogenous sources (e.g., N_2, NO_3^-) provides a promising method for urea production, whereas the current electrochemical methods are limited by low conversion efficiency or reliance on fossil fuel-derived NO_3^- feedstock. Here, we develop a plasma-electrocatalytic route for urea synthesis from ambient air and CO_2, which starts with plasma-assisted air activation to generate reactive NO_x^- (92.1% NO_2^-), followed by electrocatalytic co-reduction of $CO_2 + NO_x^-$ to urea. By using a single-atom Ru_1/CuO_x catalyst in double chamber membrane electrode assembly, we achieve a urea yield rate of 106.9 mmol h^{-1} g_{cat}^{-1} and a Faradaic efficiency of 86.7%. This plasma-electrocatalytic route demonstrates a paradigm-shifting strategy for revolutionizing urea synthesis, making a great leap toward decarbonized nitrogen economy.

Urea is a vital nitrogen carrier for fertilizers and chemicals[1]. Conventional urea production depends on the energy-intensive Bosch-Meiser process, resulting in huge energy consumption and massive CO_2 emission[2]. Electrocatalytic co-reduction of N_2 and CO_2 offers a promising pathway for sustainable urea production[3], whereas its practical viability is hindered by strong N ≡ N bond (941 kJ mol^{-1}) and ultralow N_2 solubility, resulting in rather low urea Faradaic efficiencies (FE_{urea})[4–6]. Compared to N_2, nitrogen oxides (NO_x^-), such as NO_2^- and NO_3^-, exhibit much weaker N = O bond (204 kJ mol^{-1}) and better aqueous solubility, making NO_x^- a promising alternative nitrogen source for urea electrosynthesis via co-reduction of NO_x^- and CO_2[7–11]. However, the NO_x^- feedstock relies predominantly on the fossil fuel-dependent Ostwald process with high carbon emissions, thereby compromising the sustainability and decarbonization of electrocatalysis process[12].

Recent breakthrough in non-thermal plasma technology has unveiled a paradigm-shifting strategy for revolutionizing urea synthesis via a plasma-electrocatalytic pathway (Fig. 1a), which involves plasma-assisted air activation (pAA) to generate NO_x^- and followed electrocatalytic co-reduction of plasma-derived NO_x^- and CO_2 to urea (eNCU)[13–15]. By leveraging plasma-driven air activation, the initial pAA process overcomes the thermodynamic challenges of N ≡ N bond cleavage in atmospheric N_2, generating reactive NO_x species that are subsequently absorbed in alkaline solution to yield NO_x^- solution dominated by NO_2^-[16,17]. The preferential NO_2^- formation confers a critical advantage for eNCU process, as $CO_2 + NO_2^-$ co-electrolysis proceeds via a 12-electron transfer process, significantly enhancing reaction kinetics and FE_{urea} for urea synthesis compared to a 16-electron pathway for $CO_2 + NO_3^-$ co-electrolysis[18]. In addition, pAA-eNCU route exclusively utilizes atmospheric air as nitrogen resource, circumventing fossil fuel dependency and enabling a self-sustaining nitrogen cycle. By harmonizing renewable electricity with air-derived nitrogen reactants, pAA-eNCU pioneers a closed-loop route for sustainable agrochemical and chemical manufacturing, representing a great leap toward decarbonized nitrogen economy.

Herein, we introduce a pAA-eNCU route for green and efficient urea synthesis. The first pAA process enables the effective air-to-NO_x^- conversion with NO_2^- selectivity of 92.1% and NO_x^- yield rate of up to 128.7 mM h^{-1}. A single-atom Ru_1/CuO_x catalyst comprising isolated Ru confined in oxygen-vacancy-rich CuO_x is then designed as an effective dual-active-site platform to catalyze eNCU process. Impressively, Ru_1/CuO_x assembled into a double chamber membrane electrode assembly (DCMEA) cell achieves the maximum urea yield rate of

[1]School of Materials Science and Engineering, Lanzhou Jiaotong University, Lanzhou, China. [2]MOE Key Laboratory of New Processing Technology for Nonferrous Metals and Materials, Guangxi Key Laboratory of Processing for Non-ferrous Metals and Featured Materials, School of Resources, Environment and Materials, Guangxi University, Nanning, Guangxi, China. [3]School of Materials Science and Engineering, University of Science and Technology Beijing, Beijing, China. ✉e-mail: xjliu@gxu.edu.cn; fenglb@lzjtu.edu.cn; chuk630@mail.lzjtu.cn

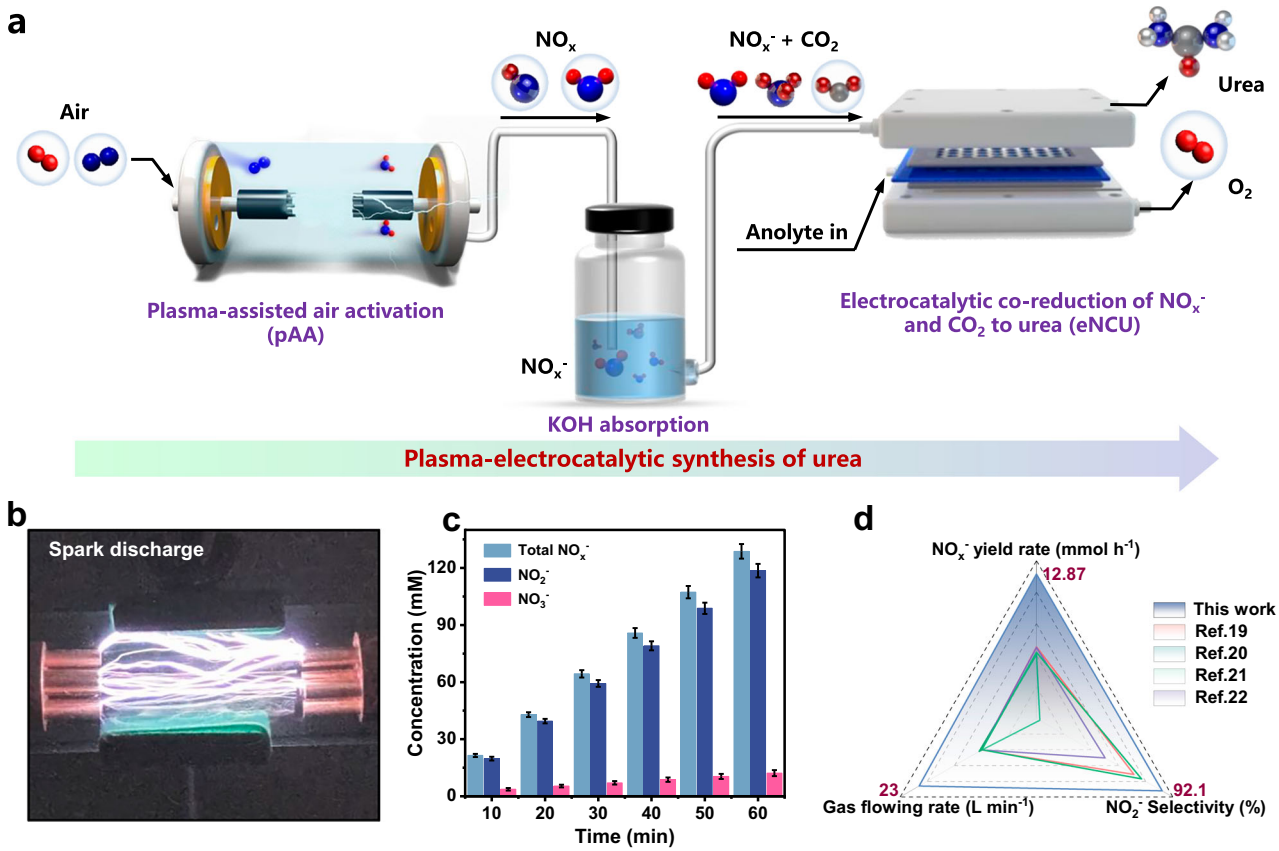

Fig. 1 | Investigations of pAA-eNCU pathway. a Schematic of plasma-electrocatalytic (pAA-eNCU) pathway. **b** Photograph of plasma discharge. **c** Effect of discharge time on the resulting concentrations of generated NO_x^- (NO_2^-/NO_3^-) and NO_2^- selectivity. **d** Comparison of the performances between our method and reported data for pAA-derived NO_x^-. Source data are provided as a Source Data file.

106.9 mmol h^{-1} g_{cat}^{-1} with an FE_{urea} of 86.7%, surpassing nearly all previously reported performances.

Results and discussion

Plasma-assisted air activation to generate NO_x^-

For pAA process, we develop a pulsed high-voltage plasma discharge (PHPD) device assembled with multiple parallel copper columnar electrodes, which can increase the likelihood of collisions between N and O radicals to enhance the NO_x production rate. During each discharge cycle (Supplementary Fig. 1), PHPD device generates a brilliant arc discharge between the electrode tips when a 22 V DC voltage is applied (Fig. 1b). The plasma discharge effectively dissociates N_2 and O_2 molecules into reactive N and O radicals, consequently leading to the formation of NO_x gas through the recombination of N and O radicals. After continuous discharge for 5 min (Supplementary Fig. 2), the initially colorless air is changed to a reddish-brown NO_x, visually confirming the successful synthesis of NO_x gases. These generated NO_x gases are then absorbed into an alkaline KOH solution, resulting in the generation of NO_x^- (NO_2^-/NO_3^-) ions. The concentrations of the resultant NO_2^- and NO_3^- are quantified using UV–vis absorption spectroscopy (Supplementary Fig. 3).

Under the optimized flow rate of 23 L min^{-1} (Supplementary Fig. 4a) and using 0.5 M KOH absorbent (Supplementary Fig. 4b), the prolonged plasma treatment exhibits a linear increase in NO_x^- concentration up to 128.7 mM after 1 h discharge (Fig. 1c and Supplementary Fig. 5). In addition, the long-term (Supplementary Fig. 6) and cycling (Supplementary Fig. 7) stability tests confirm that pAA enables the reliable and stable NO_x^- production. Notably, our pAA delivers a favorable air-to-NO_x^- performance, surpassing most reported values in terms of air-to-NO_x^- conversion efficiency and NO_2^- selectivity (Fig. 1d and Supplementary Table 1)[19–22]. Therefore, our pAA process provides an efficient and environmentally-friendly nitrogen source for downstream urea electrosynthesis.

Catalyst characterizations

Ru_1/CuO_x catalyst used for the eNCU was synthesized via a three-step process of hydrothermal synthesis, calcination and plasma treatment (Fig. 2a). The X-ray diffraction (XRD) patterns (Supplementary Fig. 8) show that Ru_1/CuO_x exhibits the characteristic peaks of CuO (PDF#72-0629) without any Ru-related peaks, indicating that Ru species are highly dispersed within the CuO_x matrix. Scanning electron microscopy (SEM, Supplementary Fig. 9) images and transmission electron microscopy (TEM, Fig. 2b) reveal that both Ru_1/CuO_x and CuO display an irregular sheet-like morphology. High-resolution TEM (HRTEM, Fig. 2b, inset) image of Ru_1/CuO_x shows a lattice fringe of 0.28 nm, corresponding to (110) plane of CuO (Supplementary Fig. 10). Plasma treatment induces nanoscale defects or oxygen vacancies (OVs) on CuO_x, as evidenced by electron paramagnetic resonance (EPR) measurements (Supplementary Fig. 11) and X-ray photoelectron spectroscopy (XPS, Supplementary Fig. 12). Aberration-corrected high-angle annular dark-field scanning transmission microscopy (AC-HAADF-STEM, Fig. 2c) image displays numerous isolated bright dots, indicative of atomically dispersed Ru atoms on CuO_x. The isolated Ru dispersion is further confirmed by the intensity line scanning and 3D intensity profiles (Fig. 2d). Elemental mapping images verify the uniform Ru distribution across the CuO_x substrate (Fig. 2e).

Comprehensive X-ray absorption spectroscopy (XAS) studies are conducted to elucidate the coordination environment and chemical state of Ru_1/CuO_x. The X-ray absorption near-edge structure (XANES) spectra (Fig. 2f) indicate that the Ru K-edge of Ru_1/CuO_x positively

https://doi.org/10.1038/s41467-025-63923-z

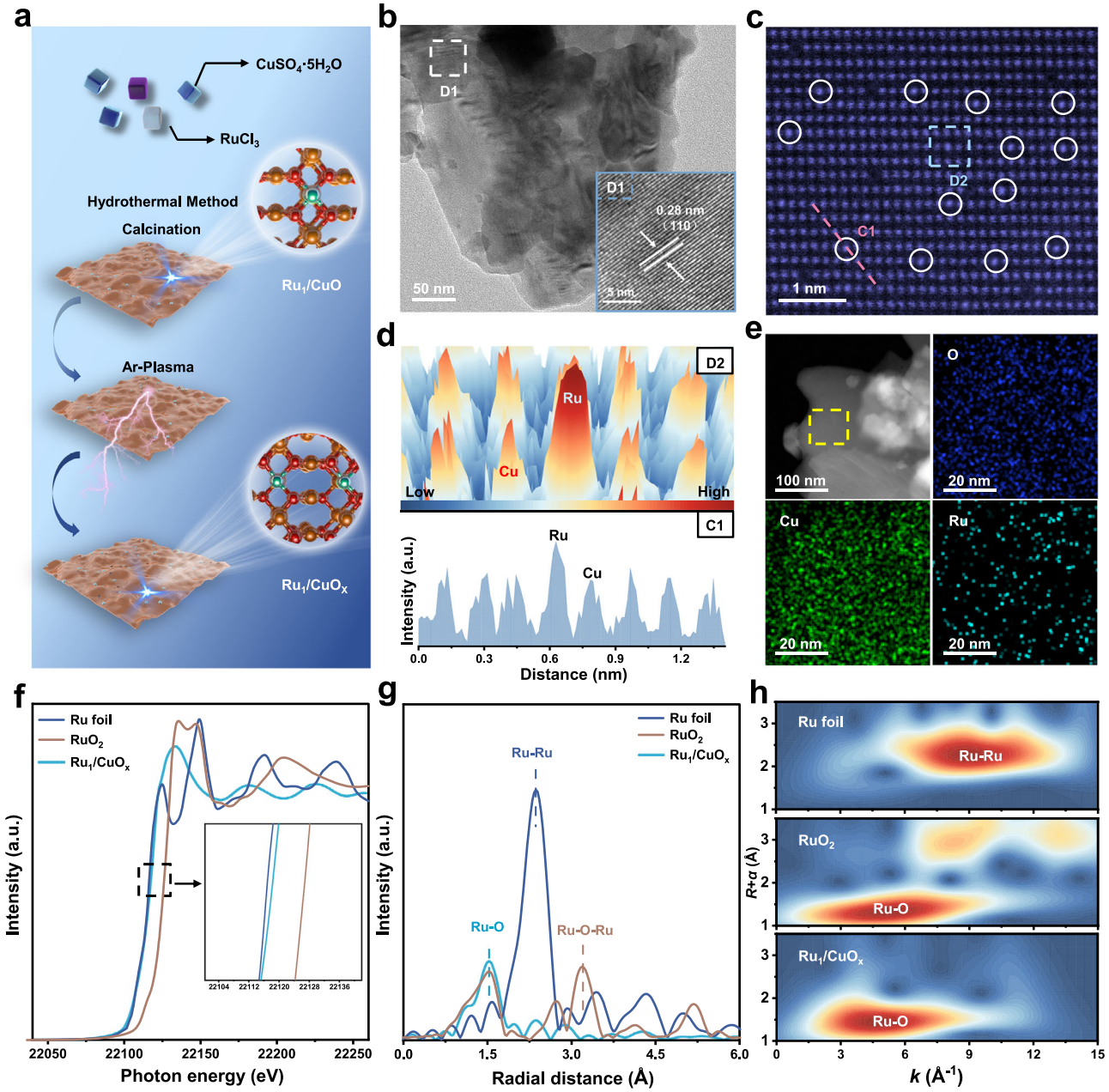

Fig. 2 | Characterization of Ru_1/CuO_x catalyst. a Schematic of Ru_1/CuO_x synthesis process. **b**–**e** Characterizations of Ru_1/CuO_x: **b** TEM image and HRTEM image (inset), **c** AC-HAADF-STEM image and corresponding **d** 3D intensity profile and atomic intensity line scanning, **e** Element mapping images. **f** Ru K-edge XANES, **g** EXAFS, and **h** WT analyses of Ru_1/CuO_x and reference samples. Source data are provided as a Source Data file.

shifts compared to Ru foil, suggesting a valence state between Ru^0 and Ru^{4+}, with an average valence state of +0.51 as determined by a linear XANES fitting analysis (Supplementary Fig. 13). The X-ray absorption fine structure (EXAFS) spectra (Fig. 2g) reveal the dominant Ru-O coordination at 1.52 Å without Ru-Ru coordination, confirming the single-atomic dispersion of Ru on CuO_x. Meanwhile, the wavelet transform (WT) contour maps (Fig. 2h) display a single Ru-O intensity maximum at 4.67 Å^{-1} with no Ru-Ru signal at 9.17 Å^{-1}, further confirming the isolated dispersion of Ru on CuO_x. In addition, the distinct differences in EXAFS spectra (Supplementary Fig. 14) and WT signals between Ru_1/CuO_x and RuO_2 reference exclude the presence of RuO_2 species on Ru_1/CuO_x. Quantitative EXAFS fitting analysis (inset, Supplementary Fig. 15 and Supplementary Table 2) indicates a Ru-O coordination number of approximately 3, suggesting that Ru atoms substitute OV-induced three-fold coordinated Cu sites of CuO_x to form a Ru_1-O_3 motif. Moreover, compared to pristine CuO, Ru_1/CuO_x shows a slight negative shift in the XANES spectra (Supplementary Fig. 16a) as well as the reduced Cu-O bond intensity (Supplementary Fig. 16b) and attenuated WT signals (Supplementary Fig. 16c), implying the unoccupied Cu states in Ru_1/CuO_x due to the presence of OVs[23,24].

Density functional theory (DFT) calculations reveal that Ru_1/CuO_x has a significantly lower formation energy of −1.8 eV compared to OV-free Ru_1/CuO (2.6 eV), highlighting the critical role of OVs in favorably confining Ru single atoms (Supplementary Fig. 17). Charge density difference maps (Supplementary Figs. 18 and 19) show strong Ru-O electronic interactions within the Ru_1-O_3 motif[25]. This is further confirmed by the partial density of states (PDOS, Supplementary Fig. 20) analysis. The ab initio molecular dynamics (AIMD, Supplementary Fig. 21) simulations show stable structural integrity (Supplementary Fig. 22), affirming the high thermodynamic stability of Ru_1/CuO_x.

https://doi.org/10.1038/s41467-025-63923-z

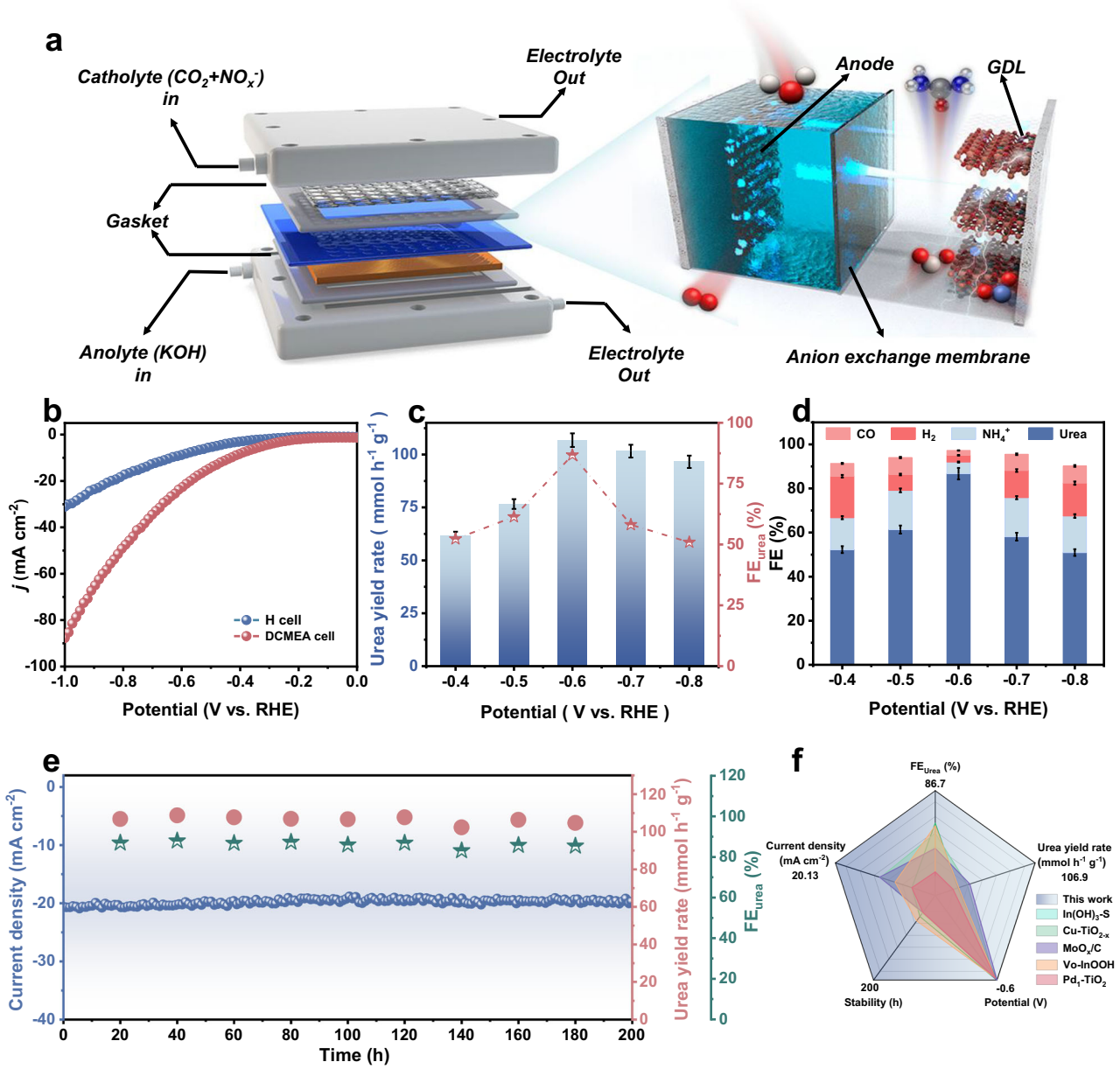

Fig. 3 | Electrochemical performance of Ru_1/CuO_x in DCMEA cell. a Schematic of the DCMEA cell. **b** LSV curves of Ru_1/CuO_x in different cells. The potential value is non-iR corrected. **c** Urea yield rate and FE_{urea} of Ru_1/CuO_x at various potentials in DCMEA cell. **d** FEs of various products on Ru_1/CuO_x. **e** Chronoamperometry tests of Ru_1/CuO_x at −0.6 V for 200 h and corresponding urea yield rates and FE_{urea} at different times. **f** Comparison of the eNCU performance between Ru_1/CuO_x and reported catalysts. Error bars represent the standard deviation of three independent samples. Source data are provided as a Source Data file.

Additionally, Ru_1/CuO_x shows more occupied electron states crossing the Fermi level (Supplementary Fig. 23) and reduced work function (Supplementary Fig. 24), indicating the enhanced electron transport capability to boost the electrocatalytic kinetics.

Electrochemical eNCU performance

The electrochemical eNCU activity of Ru_1/CuO_x is initially assessed using an H-cell containing pAA-derived NO_x^- solution (diluted to 0.1 M) + 0.1 M $KHCO_3$ saturated with CO_2[26]. The gaseous products are analyzed by gas chromatography, while liquid products are analyzed via colorimetric methods (Supplementary Fig. 25). The linear scanning voltammetry (LSV, Supplementary Fig. 26a) curves of Ru_1/CuO_x in CO_2-saturated electrolyte reveal a relatively higher current density (*j*) than that in Ar-saturated electrolyte, indicating that Ru_1/CuO_x is catalytically active for the eNCU. Chronoamperometric test (Supplementary Fig. 27) is then performed for 1 h electrolysis to quantitatively evaluate the catalytic eNCU performance of Ru_1/CuO_x. As shown in Supplementary Fig. 26b, Ru_1/CuO_x exhibits the highest FE_{urea} of 31.5% at −0.6 V with the corresponding urea yield rate of 17.1 mmol h^{-1} g_{cat}^{-1}. In addition, Ru_1/CuO_x exhibits the high stability during 30 h of electrolysis (Supplementary Fig. 26c).

The limited CO_2 mass transfer and low solubility in H-cell significantly hinder the eNCU activity. To this end, we specifically design a DCMEA cell (Fig. 3a), leveraging its low resistance, energy efficiency, and compact design to further enhance the eNCU efficiency for urea electrosynthesis[27,28]. Fig. 3b shows that Ru_1/CuO_x in DCMEA cell exhibits a markedly higher current density compared to that in H cell. When operated at −0.6 V, Ru_1/CuO_x-DCMEA system delivers a remarkable urea yield rate of 106.9 mmol h^{-1} g_{cat}^{-1} and FE_{urea} of 86.7% (Fig. 3c and Supplementary Fig. 28), significantly outperforming those obtained in H cell (Supplementary Fig. 29) and ranking among nearly the best performances to date (Fig. 3f, Supplementary Fig. 30 and

Supplementary Table 3). Fig. 3d shows that FEs of byproducts (NO_2^-, NH_3, CO, and H_2) are significantly lower than FE_{urea} at the optimal potential of −0.6 V, highlighting the excellent selectivity of Ru_1/CuO_x for NO_x^-/CO_2-to-urea conversion. In addition, pristine CuO_x shows a significantly lower eNCU activity than Ru_1/CuO_x under the identical condition (Supplementary Fig. 31), confirming the crucial role of Ru_1 incorporation in enhancing the eNCU performance. Meanwhile, we prepare Fe_1/CuO_x and Ni_1/CuO_x catalysts using the same method and the results (Supplementary Figs. 32–35) show that both catalysts exhibit the substantially lower urea yield rates and selectivities than Ru_1/CuO_x, clearly demonstrating that Ru has a unique ability to simultaneously enhance both catalytic activity and selectivity.

To trace urea origins, the nuclear magnetic resonance (NMR) experiments using $^{13}CO_2$ and $^{15}NO_2^-$ (Supplementary Figs. 36 and 37) confirm that the produced urea is derived from the Ru_1/CuO_x-catalyzed eNCU process[29]. This result is further confirmed by the various controlled measurements (Supplementary Fig. 38) and switching cycling test with and without CO_2 or NO_x^- (Supplementary Fig. 39). Finally, the electrocatalytic stability of Ru_1/CuO_x during eNCU electrolysis is thoroughly evaluated. A 30-cycle experiment (Supplementary Fig. 40) presents slight fluctuations in FE_{urea} and urea yield rates, confirming strong cycling durability of Ru_1/CuO_x. The current density shows a negligible variation during 200 h continuous electrolysis (Fig. 3e), confirming the outstanding long-term stability of Ru_1/CuO_x. Post-electrolysis analysis confirms that Ru_1/CuO_x maintains its original structure and morphology (Supplementary Figs. 41 and 42), demonstrating its robust structural stability.

Mechanistic catalysis investigations

Theoretical computations are employed to elucidate the eNCU mechanism of Ru_1/CuO_x. Since NO_2^- is the primary component of NO_x^- (92.1%, Fig. 1e), we primarily analyze $NO_2^- + CO_2$ co-reduction process. Based on the prior XAS and DFT results, four potential active sites on Ru_1/CuO_x are analyzed: pristine Cu site, pristine Ru_1 site, OV-adjacent Cu site (Cu-OV) as well as OV-adjacent Ru_1 site (Ru_1-OV). Initial adsorption studies (Fig. 4a and Supplementary Fig. 43) reveal that NO_2^- binds more strongly on Ru_1-OV site compared to Ru_1 site, while CO_2 binds more strongly on Cu-OV site compared to Cu site (Fig. 4b). This is attributed to the electron-rich OVs which can effectively activate CO_2 (Supplementary Figs. 44–46) and NO_2^- (Supplementary Figs. 47–49), enhancing their adsorption on the catalyst surface[30,31]. Therefore, Ru_1-OV and Cu-OV serve as the active sites to catalyze NO_2^- and CO_2, respectively, during the eNCU process on Ru_1/CuO_x.

To examine the energy-favored eNCU pathway on Ru_1/CuO_x, online differential electrochemical mass spectrometry (DEMS) measurements test is firstly performed to identify the crucial eNCU intermediates. The online DEMS measurements (Supplementary Fig. 50) identify the presence of key intermediates of $*CONH_2$, $*NH_2$, and *CO while excluding *CONHO, indicating that *CO and $*NH_2$ are the critical intermediates for C-N coupling towards the urea synthesis. Examining the energetic $CO_2 \rightarrow *CO$ pathway on Cu-OV and Ru_1-OV sites (Fig. 4c and Supplementary Fig. 51) reveals that Cu-OV site prefers to drive $CO_2 \rightarrow *CO$ process. Conversely, $NO_2^- \rightarrow *NH_2$ process is energetically more favorable on Ru_1-OV site (Fig. 4d and Supplementary Fig. 52). Subsequent analysis of the C-N coupling between *CO and $*NH_2$ reveals that *CO migration from Cu-OV site to Ru_1-OV site is energetically more preferred (Supplementary Figs. 53 and 54), facilitating the subsequent C-N coupling with $*NH_2$ on Ru_1-OV towards the urea formation. This is further directly confirmed by the free energy profiles (Fig. 4e and Supplementary Figs. 55 and 56), revealing that C-N coupling ($*NH_2 + *CO \rightarrow *CONH_2$) is energetically more downhill on Ru_1-OV site compared to Cu-OV site (Supplementary Figs. 57 and 58).

Since NO_2^- reduction to NH_3 (NO_2RR) and hydrogen evolution reaction (HER) serve as two predominant competitive reactions for the eNCU[32,33], we analyze the NO_2RR and HER behaviors of Ru_1/CuO_x to evaluate its eNCU selectivity. For NO_2RR, as shown in Supplementary Figs. 59 and 60, the free energy of $*NH_2/CO_2$ coupling is much lower than that of $*NH_2$ hydrogenation to NH_3, suggesting that the competing NO_2RR can be well hampered on Ru_1/CuO_x. Regarding the HER, the free energy calculations (Supplementary Fig. 61) indicate that Ru_1-OV site prefers to bind NO_2^- rather than H, while Cu-OV site prefers to bind CO_2 rather than H. A preferential adsorption of NO_2^- and CO_2 over H suggests the effective HER suppression on Ru_1/CuO_x. Molecular dynamics (MD) simulations (Supplementary Figs. 62–65) further support these findings, showing significant NO_2^- accumulation around Ru_1/CuO_x and stronger catalyst-NO_2^- interaction over catalyst-H interaction. These results demonstrate that the competing NO_2RR and HER are both effectively suppressed on Ru_1/CuO_x, enabling the achievement of high eNCU selectivity for urea synthesis.

To experimentally validate the above theoretical predictions, in situ FTIR and Raman measurements are conducted during the eNCU electrolysis from open circuit potential (OCP) to −0.6 V. For Ru_1/CuO_x (Fig. 4f), the infrared band at 2039 cm^{-1} corresponds to C = O bond, while the band at 1290 cm^{-1} is assigned to *COOH. The infrared bands at 1167 and 1085 cm^{-1} correspond to the bending and rocking modes of $-NH_2$ in urea, respectively[7,34]. Notably, the signals at 1415 cm^{-1} (C-N coupling bond) and 1634 cm^{-1} ($*CONH_2$) confirm the formation of C-N bonds[35]. The intensity of C-N bond (1415 cm^{-1}) progressively increases with increasing the applied potential, indicating the exceptional eNCU performance of Ru_1/CuO_x to drive the C-N coupling process (Supplementary Fig. 66). In contrast to Ru_1/CuO_x, pristine CuO_x (Fig. 4g and Supplementary Figs. 67 and 68) shows much weaker signals of C-N bonds and urea-related species, highlighting the critical role of Ru_1 in facilitating $*NH_2$ generation and C-N coupling. The boosted C-N coupling can be further proved by the in situ Raman spectra (Fig. 4h and Supplementary Figs. 69 and 70)[36], presenting a much enhanced N-C-N bond intensity on Ru_1/CuO_x compared to that on CuO_x. These collected theoretical calculations and in situ spectroscopic data demonstrate that Ru_1/CuO_x efficiently catalyzes eNCU through a synergistic catalysis mechanism (Fig. 5a), in which Cu-OV site preferentially activates CO_2 to *CO, while Ru_1-OV site activates NO_2^- to $*NH_2$. The *CO migration from Cu-OV site to Ru_1-OV site facilitates selective C-N coupling with $*NH_2$ towards the urea generation.

Energy consumption and techno-economic analyses

To demonstrate the application potential of our pAA-eNCU approach, we conduct a comprehensive comparison with conventional urea synthesis methods (Supplementary Notes 1–3). Specifically, our pAA-eNCU process exhibits a urea synthesis energy consumption of 73.1 MJ/kg, 31.5% higher than industrial process but 65.9% lower than conventional electrocatalytic urea synthesis from NO_3^- and CO_2 (Supplementary Note 1). Crucially, pAA-eNCU achieves 78.3% and 74.8% reductions in carbon emission compared to industrial process and conventional electrocatalytic urea synthesis method (Supplementary Note 1), respectively, demonstrating the outstanding energy efficiency and low-carbon footprint of our pAA-eNCU route. Furthermore, a comprehensive techno-economic analysis (TEA, Fig. 5b and Supplementary Note 2) reveals that our pAA-eNCU route becomes economically viable when the electricity price is less than US$0.03 per kWh and FE_{urea} surpasses 80% at a current density of 0.3 A cm^{-2} (Fig. 5c). These findings demonstrate that our pAA-eNCU shows great potential as an economical and sustainable strategy for practical application.

In summary, we have successfully developed a plasma-electrocatalytic pathway (pAA-eNCU) for green urea synthesis, which integrates plasma-assisted air activation with the co-electrolysis of NO_x^- and CO_2, consequently overcoming the low urea synthesis efficiency or indirect carbon emissions associated with the conversional urea synthesis methods. Notably, Ru_1/CuO_x assembled into a DCMEA cell achieves the maximum urea yield rate

https://doi.org/10.1038/s41467-025-63923-z

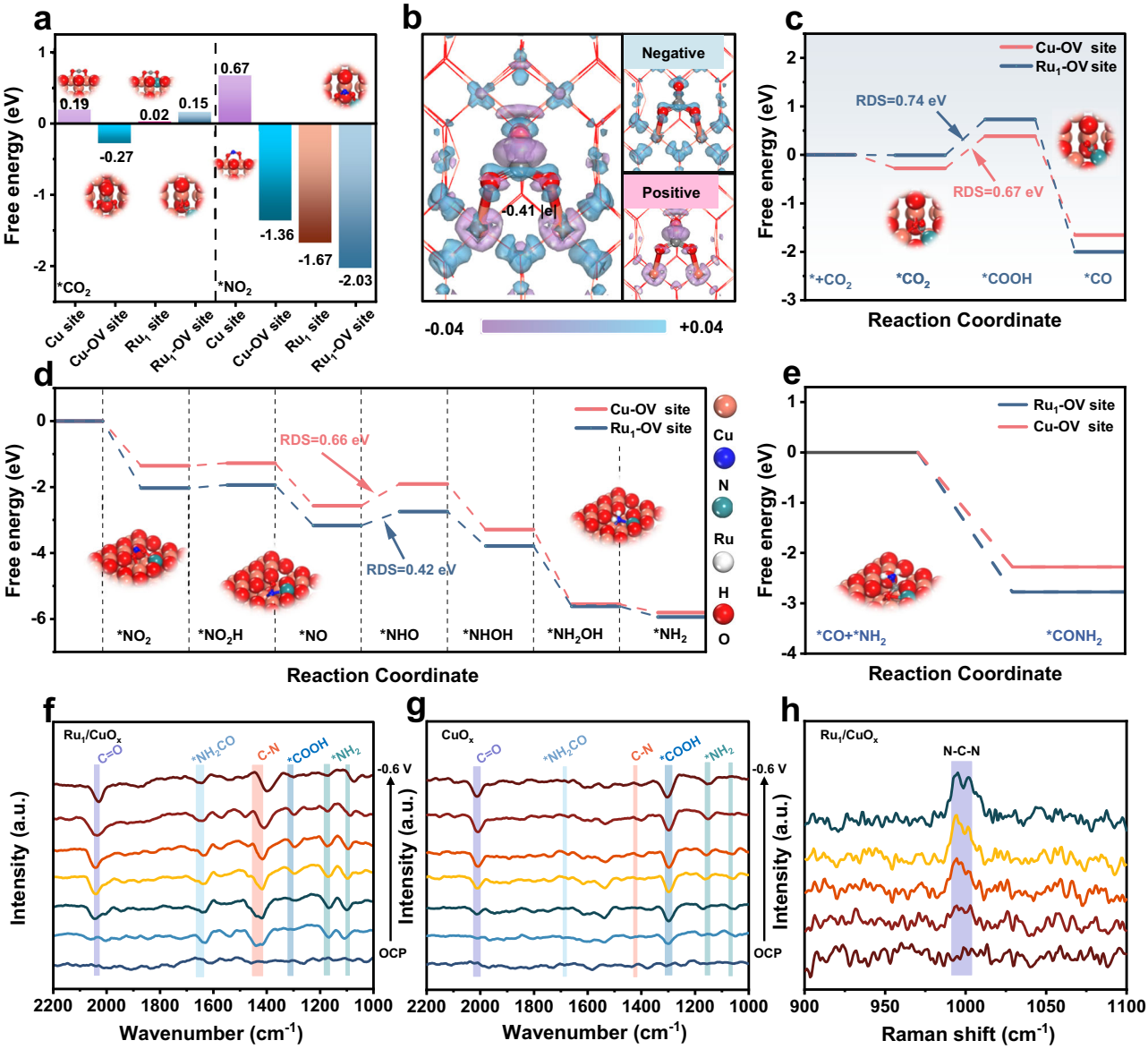

Fig. 4 | Mechanistic eNCU investigations. a Adsorption free energies of $*NO_2$ and $*CO_2$ on different sites of Ru_1/CuO_x. **b** Charge density difference map of $*CO_2$ on Cu-OV site. **c**–**e** Free energy diagrams of **c** $CO_2 \rightarrow *CO$, **d** $NO_2^- \rightarrow *NH_2$ pathways, and **e** C-N coupling of *CO and $*NH_2$ on Cu-OV and Ru_1-OV sites. **f**, **g** In situ FTIR spectra of **f** Ru_1/CuO_x and **g** CuO_x during the eNCU electrolysis at different potentials. **h** In situ Raman spectra of Ru_1/CuO_x during the eNCU electrolysis at different potentials. Source data are provided as a Source Data file.

of 106.9 mmol h^{-1} g_{cat}^{-1} with an FE_{urea} of 86.7%, surpassing nearly all previously reported catalysts. Mechanistic studies reveal the synergistic effect of Ru_1-OV and Cu-OV sites to enhance NO_2^-/CO_2 activation and their C-N coupling, while simultaneously inhibiting the competing reactions. The present pAA-eNCU route paves the new way for efficient and sustainable urea synthesis, harnessing atmospheric resources and renewable energy to accelerate the global transition toward sustainable agriculture and green chemical production.

Methods

Materials

All the reagents were of analytical grade and were used as received without further purification. $CuSO_4{\cdot}5H_2O$ (≥ 99.9%), $RuCl_3{\cdot}3H_2O$ (≥ 99.9%), $C_4H_6N_2$ (≥ 99.9%), CH_4O (≥ 99.9%), NaOH (≥ 96.0%), $C_7H_6O_3$ (≥ 99.5%), KOH (≥ 99.9%), $KHCO_3$ (≥ 99.9%), NH_4Cl (≥ 99.5%), $C_6H_5Na_3O_7{\cdot}2H_2O$ (≥ 99.0%), $C_5FeN_6Na_2O{\cdot}2H_2O$ (≥ 99.0%), urease, Nafion (5 wt%) and NaClO (≥ 99.9%) were purchased from Sinopharm Chemical Reagent Co, Ltd. H_2SO_4 (98%), $N_2H_4{\cdot}H_2O$ (≥ 99.9%) and C_2H_5OH (99.0%) were purchased from Sigma-Aldrich Chemical Reagent Co, Ltd. CO_2 (≥ 99.999%) and Ar (≥ 99.999%) were provided from Lanzhou Xinwanke, Co., Ltd. All reagents were analytical reagent grade without further purification.

Plasma-assisted air activation to generate NO_x^-

A pulsed high-voltage plasma discharge (PHPD) system was utilized to activate and dissociate air molecules to generate NO_x. This system primarily comprised three key components: power regulation module, plasma reactor and gas flow control system. The power regulation module was powered by a low-voltage direct current (DC) power supply (12–24 V). A high-voltage module (Model: DC High-Voltage Modules-150KV, Guangao Technology (Wuhan) Co., Ltd) was assembled to amplify the voltage to deliver 100–150 kV pulsed outputs with less than 1 μs rise time. Pulse parameters (50–500 ns width, 1–50 Hz frequency) enable discharge dynamics. The output potential was precisely measured using a high-voltage voltmeter (Model: 69C17,

https://doi.org/10.1038/s41467-025-63923-z

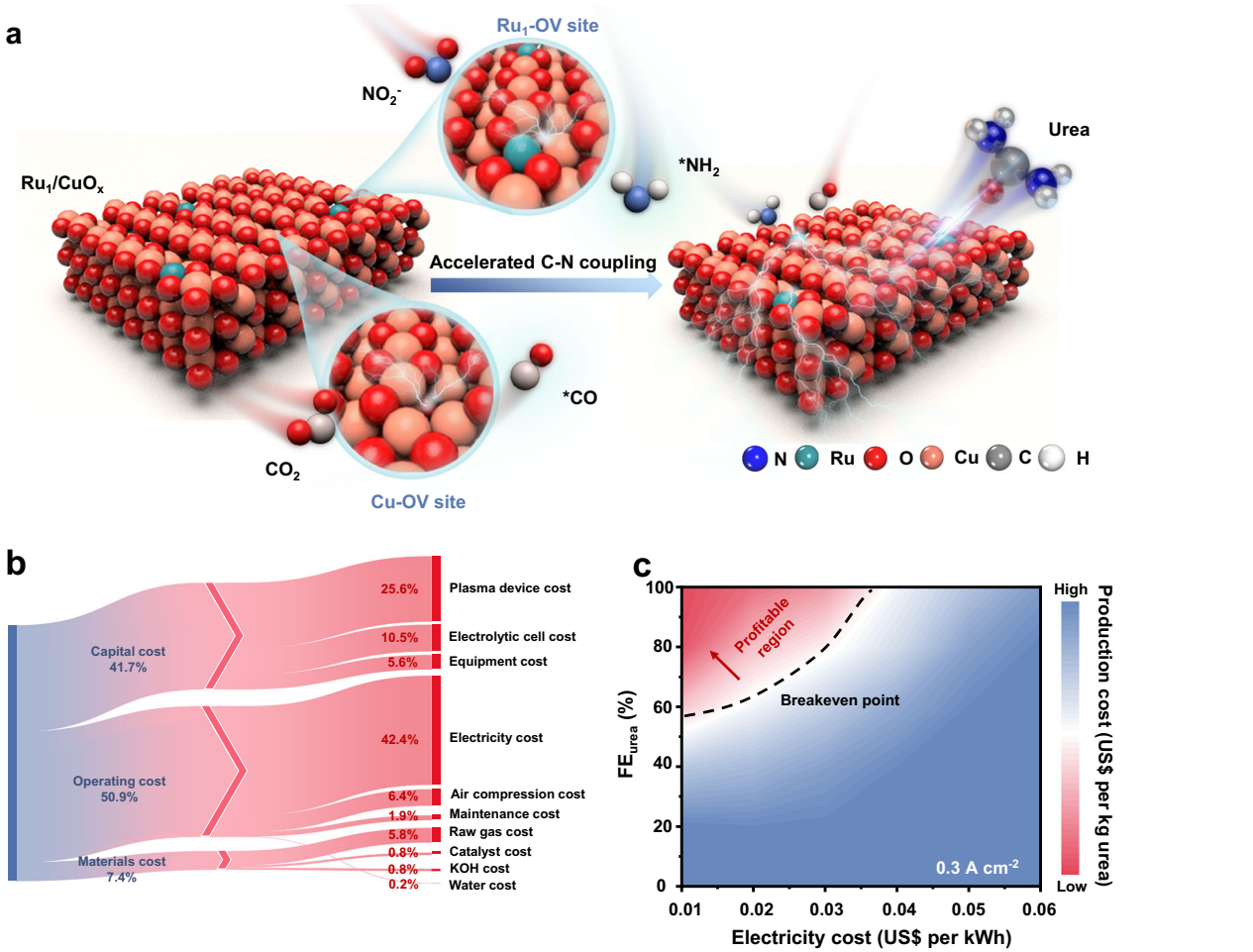

Fig. 5 | Catalytic eNCU mechanism and TEA assessment. a Schematic of the eNCU catalysis mechanism on Ru_1/CuO_x. **b** Estimated costs of pAA-eNCU route. **c** TEA for urea production of pAA-eNCU route at 0.3 A cm^{-2}. Source data are provided as a Source Data file.

Wenzhou Telun Electric Co., Ltd). The plasma reactor comprised a 20 mm inner diameter glass tube (Chemglass CG-10), incorporating two copper electrodes embedded with multiple parallel columnar (surface roughness less than 0.1 μm) spaced 2–5 mm apart to sustain filamentary discharge, and was equipped with gas inlet/outlet ports for controlled feeding and discharging of reactants. Ambient air was introduced into the plasma reactor at a controlled volumetric flow rate, regulated by the gas flow control system (Model: ACU10FD-XS, Beijing Precision Technology Co., Ltd). After a period of plasma discharge, the outlet gas was absorbed in an Erlenmeyer flask containing 0.5 M KOH solution (25 °C, pH 11), where NO_x was converted into NO_x^- ions (NO_2^-/NO_3^-). The resulting NO_2^- and NO_3^- concentrations were subsequently quantified with high precision using UV–vis absorption spectroscopy (MAPADA, P5).

Synthesis of Ru_1/CuO_x

Ru_1/CuO_x was synthesized by using the hydrothermal method. In brief, 2.0 × *g* of $CuSO_4{\cdot}5H_2O$ and 0.1 × *g* of $RuCl_3{\cdot}3H_2O$ were dissolved in 100 mL of deionized water. The mixed solution was placed in an ice-water bath with vigorous magnetic stirring to form a homogeneous blue solution. Then, 20 mL of NaOH (0.96 × *g*) solution was injected into the flask and the mixture was continuously stirred for 30 min. After being refrigerated (4 °C) for 24 h, the mixture was transferred into a Teflon-lined autoclave and heated at 130 °C for 18 h. After cooling, the obtained sediments were collected, washed, and dried overnight. Subsequently, the resulting powder was calcined at 400 °C for 3 h to obtain Ru_1/CuO. Finally, Ru_1/CuO was further subjected to Ar plasma treatment for 10 min in an AX-1000 plasma system (13.56 MHz) to obtain Ru_1/CuO_x. For comparison, CuO_x was prepared by the same as that of Ru_1/CuO_x without adding $RuCl_3{\cdot}3H_2O$.

Electrochemical experiments in H-type cell

A catalyst slurry was prepared by dissolving 25 mg of the Ru_1/CuO_x in 3 mL of isopropanol and then adding 20 μL of Nafion ionomer solution (5 wt% in H_2O). The catalyst slurry was slowly dropped onto carbon paper with an area of 1 × 1 cm^2 (0.5 mg cm^{-2}), which was used as working electrode. Ag/AgCl (in saturated KCl) and Pt foil (1 cm × 1 cm) were employed as the reference and counter electrodes, respectively. The electrolytic testing process is carried out in an H-type cell using a standard three-electrode system at room temperature (298 K) and pressure. A Nafion 117 membrane (Chemours, 2.5 × 2.5 cm^2, 183 μm in thickness) was employed as a separator between the cathode and anode compartments. Prior to use, the membrane was pretreated by sequential immersion in deionized water, a 5% H_2O_2 solution, and 0.5 M H_2SO_4 at 80 °C for 1 h each. The catholyte was a solution containing 0.1 M NO_x^- and 0.1 M $KHCO_3$ (pH = 8.47 ± 0.1), while the anolyte consisted of a 1 M KOH solution, stored in a sealed container at 25 °C. Prior to electrochemical experiments, the catholyte was purged with either CO_2 or Ar gas. During electrolysis, a continuous flow of CO_2 at a rate of 20 s.c.c.m. was supplied to the catholyte. After 1 h electrolysis at specified potentials, the produced urea was quantitatively determined using the urease decomposition method. The reported current density was normalized to the geometric area of carbon paper without iR compensation. The potentials were recalculated into

reversible hydrogen electrode (RHE) by E (V vs. RHE) = E (V vs. Ag/AgCl) + 0.198 V + 0.059 × pH. The electrochemical data in this study were not iR corrected, with all potentials reported as measured versus the reference electrode. Unless noted otherwise, all performance metrics and product quantification results represent averages from at least three independent measurements.

Electrochemical experiments in DCMEA cell

Electrochemical experiments were performed in a double-chamber membrane electrode assembly electrolyzer. The setup consisted of two titanium current collector plates (cathode and anode) with serpentine flow channels, separated by two 300 μm PTFE gaskets. The cathode slurry was prepared through sonication for 30 min after mixing 25 mg of Ru_1/CuO_x in 3 mL of isopropanol with 20 μL of Nafion ionomer solution (5 wt% in H_2O). Next, the catalyst slurry was slowly dropped onto the carbon paper (Sigracet 29 BC) to attain a catalyst loading of ~0.5 mg cm^{-2} as a gas diffusion layer (GDL). Nickel mesh was used as the anode. The cathode and anode were separated by an anion exchange membrane (Fumasep FAA-3-PK-75). The catholyte was purged with CO_2 or Ar prior to the electrochemical experiments. During the electrolysis, CO_2 gas was fed from the no-catalyst side of the GDL at a flow rate of 20 s.c.c.m., and both catholyte and anolyte were continuously cycled at a rate of 20 mL min^{-1} under pump drive. The linear sweep voltammetry (LSV) measurements were performed using a scan rate of 50 mV s^{-1}, with no applied iR correction to the potentials. All electrochemical measurements were conducted at 25 °C under ambient pressure conditions.

Product quantification

The concentrations of NO_2^-, NO_3^-, and NH_3 in electrolytes were quantified via UV–Vis spectrophotometry using colorimetric methods[37]. NO_2^- was determined by adding 0.1 mL chromogenic reagent (containing 0.1 × g N-(1-naphthyl) ethylenediamine dihydrochloride and 1.0 × g sulfanilamide in 50 mL deionized water with 2.94 mL 85% H_3PO_4) to 2 mL diluted electrolyte. After 30 min incubation, absorbance at 540 nm was measured against $NaNO_2$ standards. NO_3^- analysis involved mixing 2 mL diluted electrolyte with 40 μL 1 M HCl containing 4.0 μL 0.8% sulfamic acid, followed by 20 min incubation and absorbance measurement at 220 nm using KNO_3 calibration curves. NH_3 was detected via the indophenol blue method: 2 mL electrolyte was sequentially reacted with 2 mL 1 M NaOH containing 5% salicylic acid and trisodium citrate, 1 mL 0.05 M NaClO, and 0.2 mL 1% sodium nitroprusside. After 2 h incubation, absorbance at 655 nm was analyzed using NH_4Cl standards. The gaseous products (H_2, CO) were quantitatively analyzed using an online gas chromatograph (GC)[38]. Ultra-high-purity argon (99.999%) was used as the carrier gas to ensure optimal chromatographic resolution and detection sensitivity. Urea concentration was detected via urease decomposition method. Typically, 0.2 mL of urease solution with concentration of 5 mg mL^{-1} was added into 2 mL of urea electrolyte, and then reacted at 37 °C in constant temperature shaker for 40 min. Urea was decomposed by urease into CO_2 and two NH_3 molecules.

The product yield rate was calculated using the following equation:

$$Yield\ rate\left(mmol\,h^{-1}\,g^{-1}\right) = \frac{C*V}{M*t*m} \quad (1)$$

where C (mg mL^{-1}) is the measured concentration, V (mL) is the volume of the electrolyte, M (g mol^{-1}) is the relative molecular mass, t (h) is the reduction time, m (g) is the mass loading of the catalyst on CC.

The Faradaic efficiency of the liquid products was calculated using the following equation:

$$FE(\%) = \frac{n*F*C*V}{M*Q}*100\% \quad (2)$$

where n is the number of electron transfer, F (96500 C mol^{-1}) is the Faraday constant, C (mg mL^{-1}) is the measured concentration, V (mL) is the volume of the electrolyte, M (g mol^{-1}) is the relative molecular mass, Q (C) is the quantity of applied electricity.

The Faradaic efficiency for the gas products was calculated using the following equation:

$$FE(\%) = \frac{n*\eta*F}{Q}*100\% \quad (3)$$

where n is the number of electron transfer, η is the actual gas yield, F (96500 C mol^{-1}) is the Faraday constant, Q (C) is the quantity of applied electricity.

Characterizations. ICP-OES was performed on a PerkinElmer AVIO 500 spectrometer. X-ray diffraction (XRD) pattern was collected on a Rigaku D/max 2400 diffractometer with Cu Kα radiation (λ = 1.5418 Å, 40 kV). Scanning electron microscopy (SEM) was carried out on a ZEISS Gemini SEM-500 microscope. Transmission electron microscopy (TEM) and high-resolution transmission electron microscopy (HRTEM) were recorded on a Tecnai G2 F20 microscope. Electron paramagnetic resonance (EPR) measurements were conducted on a Bruker ESP-300 spectrometer. Aberration-corrected high-angle annular dark-field scanning transmission microscopy (AC-HAADF-STEM) was performed on a Titan Cubed Themis G^2 300 microscope. Synchrotron radiation-based XAS measurements were conducted at the BL14W1 beamline in Shanghai Synchrotron Radiation Facility (SSRF). Online differential electrochemical mass spectrometry (DEMS, QAS 100) was performed by QAS 100 spectrometer. Various products during the electrolysis reactions were monitored at different values of m/z ionic signals. In situ Raman spectroscopy analysis was carried out on a confocal Raman spectrometer (Horiba HR-800) with a wavelength of 532 nm. A piece of Pt gauze, Ag/AgCl and (filled with saturated KCl solution) and catalyst-coated CC electrode were used as the counter electrode, reference electrode, and working electrode, respectively. During the potentiostatic testing, the green laser beam was perpendicularly focused onto the working electrode and the backscattered light was collected. In situ Raman spectroscopy analysis was carried out on a confocal Raman spectrometer (Horiba HR-800) with a wavelength of 532 nm. In situ Fourier-transform infrared spectroscopy (FTIR) was performed on a Nicolet IS50 FTIR spectrometer. Catalysts deposited on carbon paper, Ag/AgCl, and Pt wire were used as the working electrode, reference electrode, and counter electrode, respectively. The Ge single crystal was used as the substrate for working electrode to ensure we can get enough IR signals. During the potentiostatic testing, the spectral signal was collected at a resolution of 4 cm^{-1} with 32 scans at each applied potential.

Calculation details. DFT calculations were carried out using the Cambridge sequential total energy package (CASTEP) with ultrasoft pseudopotentials. The exchange-correlation functional is evaluated using the Perdew-Burke-Ernzerhof (PBE) in the generalized gradient approximation. DFT-D3 method was employed to calculate the van der Waals (vdW) interactions. According to the experimental characterizations, CuO basal plane (110) has been modeled as 2 × 2 supercell. A vacuum region of 15 Å was used to separate adjacent slabs. The cutoff energy was set as 450 eV and the k-point meshes were set as 2 × 2 × 1. For DOS calculation, the k-point meshes were set as 9 × 9 × 1. The AIMD simulation was carried out to estimate the thermal stability, in which the NVT ensemble is chosen with the total simulation time of 5 ns at a time step of 1 fs. Molecular dynamics (MD) simulations were performed using the Forcite module (Supplementary Data 1). The electrolyte system was modeled by a cubic cell with placing catalyst at the center of the cell and randomly filling 1000 H_2O, 50 NO_2^-, 20 CO_2 molecules, and 50 H atoms. The force field type was chosen as

universal. After geometry optimization, the MD simulations were performed in an NVT ensemble (298 K) with the total simulation time of 5 ns at a time step of 1 fs.

Data availability

The data supporting the plots within this paper and other study findings are available from the corresponding author upon request. Source data are provided in this paper. Source data are provided with this paper.

References

1. Kohlhaas, Y. et al. Electrochemical urea synthesis. *Joule* **8**, 1579–1600 (2024).
2. Muhyuddin, M. et al. Electrochemical urea production using carbon dioxide and nitrate: state of the art and perspectives. *Energy Environ. Sci.* **17**, 3739–3752 (2024).
3. Chen, C. et al. Coupling N_2 and CO_2 in H_2O to synthesize urea under ambient conditions. *Nat. Chem.* **12**, 717–724 (2020).
4. Pan, L. et al. Single-atom or dual-atom in TiO_2 nanosheet: which is the better choice for electrocatalytic urea synthesis? *Angew. Chem. Int. Ed.* **135**, e202216835 (2023).
5. Suryanto, B. H. et al. Nitrogen reduction to ammonia at high efficiency and rates based on a phosphonium proton shuttle. *Science* **372**, 1187–1191 (2021).
6. Yuan, M. et al. Highly selective electroreduction of N_2 and CO_2 to urea over artificial frustrated Lewis pairs. *Energy Environ. Sci.* **14**, 6605–6615 (2021).
7. Lv, C. et al. Selective electrocatalytic synthesis of urea with nitrate and carbon dioxide. *Nat. Sustain.* **4**, 868–876 (2021).
8. Feng, Y. et al. Te-doped Pd nanocrystal for electrochemical urea production by efficiently coupling carbon dioxide reduction with nitrite reduction. *Nano Lett.* **20**, 8282–8289 (2020).
9. Wu, Q., Dai, C., Meng, F., Jiao, Y. & Xu, Z. J. Potential and electric double-layer effect in electrocatalytic urea synthesis. *Nat. Commun.* **15**, 1095 (2024).
10. Zhang, J. et al. Regulating reconstruction-engineered active sites for accelerated electrocatalytic conversion of urea. *Angew. Chem. Int. Ed.* **63**, e202407038 (2024).
11. Meng, N. et al. Oxide-derived core-shell Cu@Zn nanowires for urea electrosynthesis from carbon dioxide and nitrate in water. *ACS Nano* **16**, 9095–9104 (2022).
12. Xiong, H. et al. Urea synthesis via electrocatalytic oxidative coupling of CO with NH_3 on Pt. *Nat. Catal.* **7**, 785–795 (2024).
13. Li, L. et al. Efficient nitrogen fixation to ammonia through integration of plasma oxidation with electrocatalytic reduction. *Angew. Chem. Int. Ed.* **133**, 14250–14256 (2021).
14. Ding, J. et al. A cascade jet plasma oxidation-electroreduction system using Pd-Ni dual-site catalyst for sustainable ammonia production from air. *Adv. Funct. Mater.* **34**, 2410768 (2024).
15. Gao, R. et al. A bifunctional catalyst for green ammonia synthesis from ubiquitous air and water. *Adv. Mater.* **35**, 2303455 (2023).
16. Li, W. et al. Sustainable nitrogen fixation to produce ammonia by electroreduction of plasma-generated nitrite. *ACS Sustainable Chem. Eng.* **11**, 1168–1177 (2023).
17. Meng, Z. et al. Efficient ammonia production beginning from enhanced air activation. *Adv. Energy Mater.* **12**, 2202105 (2022).
18. Chen, D. et al. Electrocatalytic C-N couplings at cathode and anode. *Adv. Energy Mater.* **14**, 2303820 (2024).
19. Ren, Y. et al. Microscopic-level insights into the mechanism of enhanced NH_3 synthesis in plasma-enabled cascade N_2 oxidation-electroreduction system. *J. Am. Chem. Soc.* **144**, 10193–10200 (2022).
20. Cui, Y. et al. Coupling of $LaFeO_3$-plasma catalysis and Cu^+/Cu^0 electrocatalysis for direct ammonia synthesis from air. *Ind. Eng. Chem. Res.* **61**, 4816–4823 (2022).
21. Bian, W., Song, X., Shi, J. & Yin, X. Nitrogen fixed into HNO_3 by pulsed high voltage discharge. *J. Electrost.* **70**, 317–326 (2012).
22. Sun, J. et al. A hybrid plasma electrocatalytic process for sustainable ammonia production. *Energy Environ. Sci.* **14**, 865–872 (2021).
23. Gao, C. et al. Heterogeneous single-atom photocatalysts: fundamentals and applications. *Chem. Rev.* **120**, 12175–12216 (2020).
24. Lang, R. et al. Single-atom catalysts based on the metal-oxide interaction. *Chem. Rev.* **120**, 11986–12043 (2020).
25. Guo, W. et al. Highly efficient CO_2 electroreduction to methanol through atomically dispersed Sn coupled with defective CuO catalysts. *Angew. Chem. Int. Ed.* **60**, 21979–21987 (2021).
26. Chen, K. et al. Urea electrosynthesis from nitrate and CO_2 on diatomic alloys. *Adv. Mater.* **36**, 2402160 (2024).
27. Li, Z. et al. Electron-rich bi nanosheets promote CO_2-formation for high-performance and pH-universal electrocatalytic CO_2 reduction. *Angew. Chem. Int. Ed.* **62**, e202217569 (2023).
28. Xue, W. et al. Electrosynthesis of polymer-grade ethylene via acetylene semihydrogenation over undercoordinated Cu nanodots. *Nat. Commun.* **14**, 2137 (2023).
29. Geng, J. et al. Ambient electrosynthesis of urea with nitrate and carbon dioxide over iron-based dual-sites. *Angew. Chem. Int. Ed.* **62**, e202210958 (2023).
30. Zhang, Y. et al. Promoting electroreduction of CO_2 and NO_3^- to urea via tandem catalysis of Zn single atoms and In_2O_{3-x}. *Adv. Energy Mater.* **14**, 2402309 (2024).
31. Li, Z. et al. Synergistic electrocatalysis of crystal facet and O-vacancy for enhancive urea synthesis from nitrate and CO_2. *Appl. Catal. B* **338**, 122962 (2023).
32. Zhang, X. et al. Identifying and tailoring C-N coupling site for efficient urea synthesis over diatomic Fe-Ni catalyst. *Nat. Commun.* **13**, 5337 (2022).
33. Wei, X. et al. Dynamic reconstitution between copper single atoms and clusters for electrocatalytic urea synthesis. *Adv. Mater.* **35**, 2300020 (2023).
34. Zhang, N. et al. Lewis acid Fe-V pairs promote nitrate electroreduction to ammonia. *Adv. Funct. Mater.* **33**, 2211537 (2023).
35. Zhao, Y. et al. Efficient urea electrosynthesis from carbon dioxide and nitrate via alternating Cu-W bimetallic C-N coupling sites. *Nat. Commun.* **14**, 4491 (2023).
36. Zhang, S. et al. High-efficiency electrosynthesis of urea over bacterial cellulose regulated Pd-Cu bimetallic catalyst. *EES Catal* **1**, 45–53 (2023).
37. Li, H. et al. Ligand engineering towards electrocatalytic urea synthesis on a molecular catalyst. *Nat. Commun.* **15**, 8858 (2024).
38. Qin, X.-R. et al. Electroreduction of diluted CO_2 to multicarbon products with high carbon utilization at 800 mA cm^{-2} in strongly acidic media. *Nat. Commun.* **16**, 4447 (2025).

Acknowledgements

This work is supported by National Natural Science Foundation of China (52561042), Gansu Province Key Talent Project (2025RCXM008), Gansu Province Joint Research Fund (24JRRA859), Industrial Support Plan Project of Gansu Provincial Education Department (2024CYZC-22), and Guangxi Natural Science Fund for Distinguished Young Scholars (2024GXNSFFA010008).

Author contributions

Zeyi Sun performed the primary investigations, methodology development, data collection/analysis, and wrote the original manuscript. Rui Niu and Shiyao Shang carried out the plasma treatment. Yali Guo and Hu Zhang performed the catalyst synthesis and characterizations. Xijun Liu and Libang Feng completed the theoretical simulations. Ke Chu supervised the project and provided critical input in revising and editing the manuscript.

Competing interests
The authors declare no competing interests.

Additional information
Supplementary information The online version contains supplementary material available at https://doi.org/10.1038/s41467-025-63923-z.

Correspondence and requests for materials should be addressed to Xijun Liu, Libang Feng or Ke Chu.

Peer review information *Nature Communications* thanks the anonymous reviewer(s) for their contribution to the peer review of this work. A peer review file is available.